Phase resolved near-field mode imaging for the design of frequency-selective surfaces

Edward C. Kinzel,[1,*] James C. Ginn,[2] Robert L. Olmon,[3] David J. Shelton,[2] Brian A. Lail,[4] Igal Brener,[5] Michael B. Sinclair,[5] Markus B. Raschke,[3] and Glenn D. Boreman[1,2]

[1]Department of Physics and Optical Sciences, University of North Carolina at Charlotte, 9201 University City Blvd., Charlotte, NC 28223, USA
[2]Plasmonics Inc., 12565 Research Pkwy, Suite 300, Orlando, FL, 32826, USA
[3]Department of Physics, Department of Chemistry, and JILA, University of Colorado, 390 UCB, Boulder, CO, 80309, USA
[4]Department of Electrical and Computer Engineering, Florida Institute of Technology,150 West University Boulevard, Melbourne, FL, 32901, USA
[5]Sandia National Laboratories, P.O. 5800, Albuquerque NM, 87185 USA
[*]gboreman@uncc.edu

Abstract: Frequency-selective surfaces (FSS) are a class of metasurfaces with engineered reflectance, absorbance, and transmittance behavior. We study an array of metallic crossed dipole FSS elements in the infrared using interferometric scattering-type scanning near-field optical microscopy (*s*-SNOM). We resolve the dependence of the near-field phase on the dimensions of the elements and compare with numerical models. The combined phase and amplitude information of the underlying near-field mode distribution compared to conventional far-field absorption spectroscopy greatly improves the targeted design of frequency-selective surfaces.

©2012 Optical Society of America

OCIS codes: (160.3918) Metamaterials; (260.3060) Infrared; (180.4243) Near-field microscopy.

References and links

1. B. A. Munk, *Frequency Selective Surfaces, Theory and Design* (Wiley & Sons, 2000).
2. C. M. Rhoads, E. K. Damon, and B. A. Munk, "Mid-infrared filters using conducting elements," Appl. Opt. **21**(15), 2814–2816 (1982).
3. D. J. Shelton, J. W. Cleary, J. C. Ginn, S. L. Wadsworth, R. E. Peale, D. K. Kotter, and G. D. Boreman, "Gangbuster frequency selective surface metamaterials in terahertz band," Electron. Lett. **44**(22), 1288–1289 (2008).
4. X. Liu, T. Starr, A. F. Starr, and W. J. Padilla, "Infrared spatial and frequency selective metamaterial with near-unity absorbance," Phys. Rev. Lett. **104**, 207403 (2010).
5. J. S. Tharp, J. M. Lopez-Alonso, J. C. Ginn, C. F. Middleton, B. A. Lail, B. A. Munk, and G. D. Boreman, "Demonstration of a single-layer meanderline phase retarder at infrared," Opt. Lett. **31**(18), 2687–2689 (2006).
6. I. Puscasu, W. Schaich, and G. D. Boreman, "Resonant enhancement of emission and absorption using frequency selective surfaces in the infrared," Infrared Phys. Technol. **43**(2), 101–107 (2002).
7. J. Ginn, D. Shelton, P. Krenz, B. Lail, and G. Boreman, "Polarized infrared emission using frequency selective surfaces," Opt. Express **18**(5), 4557–4563 (2010).
8. X. Liu, T. Tyler, T. Starr, A. F. Starr, N. M. Jokerst, and W. J. Padilla, "Taming the blackbody with infrared metamaterials as selective thermal emitters," Phys. Rev. Lett. **107**(4), 045901 (2011).
9. J. C. Ginn, B. A. Lail, and G. D. Boreman, "Phase characterization of reflectarray elements at infrared," IEEE Trans. Antenn. Propag. **55**(11), 2989–2993 (2007).
10. J. Ginn, B. Lail, J. Alda, and G. Boreman, "Planar infrared binary phase reflectarray," Opt. Lett. **33**(8), 779–781 (2008).
11. J. A. Gómez-Pedrero, J. Ginn, J. Alda, and G. Boreman, "Modulation transfer function for infrared reflectarrays," Appl. Opt. **50**(27), 5344–5350 (2011).
12. X. Zhang, M. Davanço, K. Maller, T. W. Jarvis, C. Wu, C. Fietz, D. Korobkin, X. Li, G. Shvets, and S. R. Forrest, "Interferometric characterization of a sub-wavelength near-infrared negative index metamaterial," Opt. Express **18**(17), 17788–17795 (2010).
13. A. C. Jones, R. L. Olmon, S. E. Skrabalak, B. J. Wiley, Y. N. Xia, and M. B. Raschke, "Mid-IR plasmonics: near-field imaging of coherent plasmon modes of silver nanowires," Nano Lett. **9**(7), 2553–2558 (2009).

14. R. L. Olmon, M. Rang, P. M. Krenz, B. A. Lail, L. V. Saraf, G. D. Boreman, and M. B. Raschke, "Determination of electric-field, magnetic-field, and electric-current distributions of infrared optical antennas: a near-field optical vector network analyzer," Phys. Rev. Lett. **105**(16), 167403 (2010).
15. M. Schnell, A. García-Etxarri, A. J. Huber, K. Crozier, J. Aizpurua, and R. Hillenbrand, "Controlling the near-field oscillations of loaded plasmonic nanoantennas," Nat. Photonics **3**(5), 287–291 (2009).
16. J. Dorfmüller, D. Dregely, M. Esslinger, W. Khunsin, R. Vogelgesang, K. Kern, and H. Giessen, "Near-field dynamics of optical Yagi-Uda nanoantennas," Nano Lett. **11**(7), 2819–2824 (2011).
17. T. Zentgraf, J. Dorfmüller, C. Rockstuhl, C. Etrich, R. Vogelgesang, K. Kern, T. Pertsch, F. Lederer, and H. Giessen, "Amplitude- and phase-resolved optical near fields of split-ring-resonator-based metamaterials," Opt. Lett. **33**(8), 848–850 (2008).
18. P. Alonso-Gonzalez, M. Schnell, P. Sarriugarte, H. Sobhani, C. Wu, N. Arju, A. Khanikaev, F. Golmar, P. Albella, L. Arzubiaga, F. Casanova, L. E. Hueso, P. Nordlander, G. Shvets, and R. Hillenbrand, "Real-space mapping of Fano interference in plasmonic metamolecules," Nano Lett. **11**(9), 3922–3926 (2011).
19. A. García-Extarri, I. Romero, F. Javier García de Abajo, R. Hillenbrand, and J. Aizpurua, "Influence of the tip in near-field imaging of nanoparticle plasmonic modes: weak and strong coupling, regimes," Phys. Rev. B **79**(12), 125439 (2009).

1. Introduction

A frequency selective surface (FSS) consists of a periodically arranged array of resonant metallic antenna elements on a dielectric surface. FSS allows a surface's transmission, reflectivity, and absorptivity to be engineered as a function of wavelength, polarization, and angle of incidence. There are many different FSS antenna elements to choose from including patches, loops, crosses, split-ring resonators, as well as more complex variations. The behavior of the FSS is a function of the geometry of the resonant elements, the array spacing, and the materials making up the elements and the dielectric surface. FSSs were originally developed at microwave frequencies [1], but have been scaled to infrared [2] as well as THz and optical wavelengths. Several significant applications have been demonstrated at these higher frequencies for FSSs including, narrowband filters [3], "perfect" absorbers [4], quarter-wave plates [5], thermal emitters [6–8], and reflectarray antennas [9–11].

Conventionally, characterization of spatially varying phase surfaces has relied on interferometric approaches to measure reflected or transmitted phase [9,12]. Although the far-field behavior of the FSS is generally the parameter of interest, the origin of its behavior is dictated by the near-field interaction between its elements. Far-field amplitude absorption measurements alone are insufficient for their structural design and optimization of their spectral characteristics. Compared to other coupled antenna structures, an FSS in particular gains its spectroscopic properties from the details of the near-field coupling between its individual building blocks. However, the relevant details of the structural morphology, and resonances and coupling are not uniquely reflected in the far-field spectral response due to the loss in k-vector information in the near- to far-field transformation.

Capturing both the optical amplitude and phase information at high spatial resolution is critical for the design of FSSs. Here, we use interferometric scattering-type scanning near-field optical microscopy (s-SNOM). This technique has previously been used to study infrared antennas [13–16] and metamaterial elements [17] to study their underlying mode profile with phase and amplitude including dark modes [18].

In this paper we design, fabricate, and measure two FSSs in the long-wave infrared ($\lambda_0 = 10.6$ µm). The FSSs consist of loaded crossed dipole elements. One array consists of resonant elements which act as a "perfect" absorber. The second array consists of different sized elements, both larger and smaller than the resonant dimension at 10.6 µm. The latter FSS shows a significant phase ramp in the near-field as well as variations in amplitude. This agrees with the Kramers-Kronig relation, which predicts that light reflected or transmitted by a FSS will exhibit a significant phase variation at frequencies near the structure's resonance. At a single wavelength, such as a laser line, this phenomenon can be exploited for wavefront shaping by using elements with different resonant frequencies to introduce a spatially varying phase shift. Ginn et al. [9,10] used this approach to design and fabricate a planar Fresnel zone plate reflectarray in the infrared ($\lambda_0 = 10.6$ µm) by varying the sizes of the elements. Although such a reflectarray FSS suffers chromatic aberration, the phase-shifting approach can be used to provide near diffraction-limited focusing at a single wavelength [11].

We show that *s*-SNOM can resolve both the amplitude and relative phase shift in the near-field even when the absorption of the elements approaches unity. These experimental results are in agreement with simulation and far-field measurement. The *s*-SNOM technique overcomes some of the obstacles that would be encountered measuring phase variant FSSs using interferometric far-field approaches. Besides model validation, the *s*-SNOM approach is of potential interest to the metamaterial community where simulated phase is often used in place of measured phase during index extraction. It is also important to the study of high-gain nano-antennas, where the directivity is determined by the relative phasing of the elements [16].

2. Experimental setup

The *s*-SNOM setup, shown in Fig. 1, is similar to the instruments discussed in Ref [13,14]. It consists of a modified atomic-force microscope (Innova, Bruker), operated in dynamic force mode. The FSS is illuminated at an incidence angle of 60° with respect to the surface normal by a CO_2 laser beam (λ_0 = 10.6 µm). This incident beam is *s*-polarized with respect to the sample (E-field parallel to the *x*-axis in Fig. 2). It is focused by an *f*/1 aspheric lens to a spot whose width is about 65 µm across the short dimension (*x*-axis). A platinum-coated probe (Arrow-NCPt, NanoWorld) is placed at the center of the spot. The incident laser radiation excites evanescent fields bound to the FSS. The tip scatters these near-fields into the far-field by acting as an antenna which is preferentially excited by the *z*-component of the E-field (normal to the probe axis and FSS). The backscattered light is collected and collimated by the lens, and the resulting beam is combined with a reference beam and focused onto a LN_2 cooled mercury-cadmium-telluride (MCT) detector, forming a Michelson interferometer. The detector responds to the intensity of the light and the interference between the reference and scattered beams allows phase-sensitive imaging as well as homodyne amplification of the weak near-field signal [13]. A wire-grid polarizer is used to block any specularly scattered *s*-polarized light from reaching the detector. A quarter-wave plate rotates the reference beam so it can interfere with the *p*-polarized collected light from the tip. Cross-polarized excitation and detection helps to suppress the background signal and prevents the tip from being directly excited and coupling energy to the FSS [19].
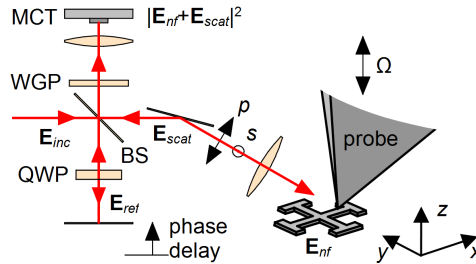

Fig. 1. Scattering-type scanning near-field optical microscope with interferometric homodyne detection.

The signal from the detector is recorded while the FSS is scanned relative to the probe (stationary in *x* and *y*, but oscillating with an amplitude of about 20 nm in the *z*-direction) and is proportional to

$$S_d \propto I = \left|E_{scat} + E_{ref}\right|^2 = \left|E_{scat}\right|^2 + \left|E_{ref}\right|^2 + 2\left|E_{scat} \cdot E_{ref}\right|\cos\varphi + I_b \qquad (1)$$

where φ denotes the phase difference between the scattered and reference beams. There is also a background signal, I_b, which results from backscattering not emanating from the tip-sample interaction and not interfering with the reference beam. This signal is demodulated at the second-harmonic of the tip dither frequency, Ω, using a lock-in amplifier. This eliminates the constant $|E_{ref}|^2$ term and when the reference beam is much more intense (~10 × - limited

by the range of the detector) than the scattered near-field the measured signal will be proportional to the last term two terms of Eq. (1). The relative phase difference is controlled by adjusting the length of the reference leg. We collect images at a series of reference phases and use a least-squares approach on point-by-point basis to extract only the data that varies with respect to reference phase, suppressing the background.

3. FSS design and fabrication

Prior to fabrication, the FSS was modeled using a commercial finite-element code simulator, Ansoft HFSS. Figure 2 shows the geometry of the FSS. The aluminum crosses are $t = 75$ nm thick and are separated from an optically thick aluminum ground plane layer by an $h = 1.2$ µm thick layer of benzo-cyclobutene (BCB) (Dow Cyclotene 3022-35 resin). BCB was selected because of its ease of deposition via spin coating, as well as its relatively low loss at infrared wavelengths. The cross-arm width of the wires was constant at $w = 0.25$ µm as was the end-cap length of $b = 0.75$ µm.
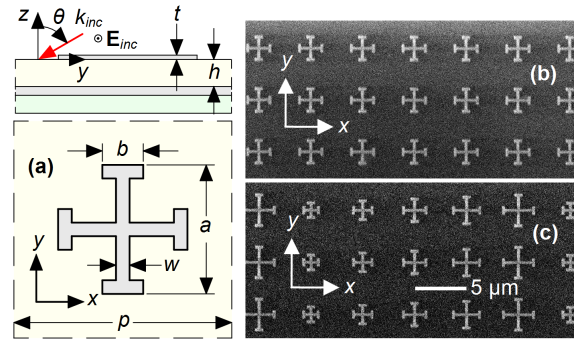

Fig. 2. FSS geometry. (a) Definition of geometric parameters of FSS, and SEM images of (b) uniformly-sized resonant crosses and (c) five-element phase ramp.

In the numerical model, frequency-dependent properties (measured with ellipsometry) were used for the BCB and aluminum. At 10.6 µm, BCB has complex index of refraction $n + ik = 1.557 + i0.0215$, and aluminum has $(n, k) = (23.86, 46.10)$. Figures 3(a) and 3(b) show the magnitude and phase of the reflectivity as a function of element length and parameterized on periodicity, calculated for the case of an infinite uniform array that is illuminated at an angle of incidence of 60° with s-polarized radiation, corresponding to the experimental s-SNOM conditions. The ground plane prevents any transmission through the structure. Hence light that is not specularly reflected is either absorbed by the FSS or diffracted. Figure 3(a) shows that each periodicity has a corresponding resonant dimension, a, and that increased spacing between elements results in a larger resonant element size. According to the numerical model, the $p = 5$ µm case results in the minimum reflectivity which is less than 0.01 when $a = 2.375$ µm. Figure 3(b) shows that there is more than a 180° phase shift in the reflected radiation for the FSSs with 2-4 µm periodicity. For larger periodicities the phase shift is less due to diffraction. From modeling and theory, the phase change with respect to element size is slower when the system is detuned from resonance [9].

To experimentally verify the effect of changing element size we fabricated two samples, SEM images of which are shown in Figs. 2(b) and 2(c). A fixed unit-cell spacing, in both x- and y- directions, $p = 5$ µm was selected because it provides the maximum absorptivity with minimal grating lobes ($< \lambda_0/2$) [10]. For this structure the near-field intensity scales with the absorbance. The first sample consists of the uniform resonant elements, where $a = 2.375$ µm. The second sample consists of five different- sized elements in a ramp array: $a = 1.625$, 2.000, 2.375, 2.750 and 3.125 µm. The five element pattern repeats in the x-direction. Even though the periodicity is constant the intra-element spacing varies along with the size of the neighboring elements, so we cannot expect the phase shifts of the off-resonant elements to be identical to the case of uniform elements and periodicity in Fig. 3. Because of the high (near-

perfect) level of absorbance the designed phase ramp would not serve as a good reflectarray, where a figure of merit is high reflectance; however, it serves well to illustrate the resonance induced phase difference with maximum near-field intensity.
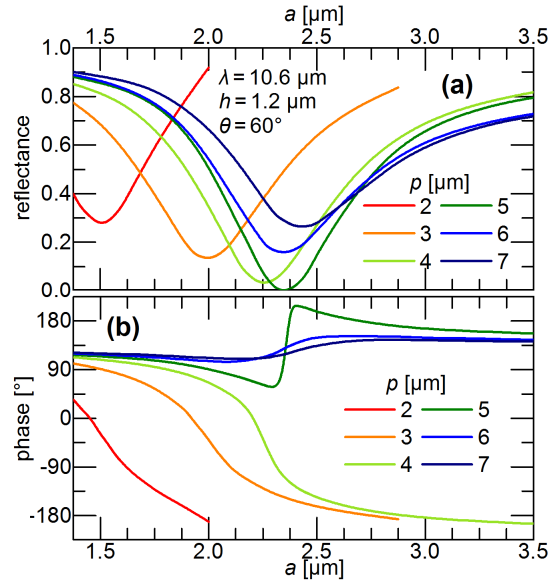

Fig. 3. Numerical modeling of an infinite FSS for *s*-polarized, 60° off-normal λ = 10.6 µm illumination: (a) reflectivity and (b) reflected phase.

The samples were fabricated using e-beam lithography. An aluminum groundplane 150 nm thick was deposited using e-beam evaporation on a Si substrate. BCB was spun onto the surface of the Al at a speed of 3500 RPM and baked for 5 min on a hot plate for a cured thickness of 1.2 µm. ZEP 520-A7, a high-resolution positive-tone e-beam resist was then spun on top of the BCB and the patterns were written by a Leica EBPG5000 + system. After development the aluminum was deposited using e-beam evaporation and lifted off. Each pattern is 2 × 2 mm in overall dimensions.

4. Results

We measured the reflectance from the uniform p = 5 µm, a = 2.375 µm FSS sample using FTIR (Perkin-Elmer). In this case the light is predominately normally incident to the FSS and unpolarized (the symmetry of the crosses makes the FSS polarization insensitive under normal illumination). Figure 4(a) shows the measured reflectivity as well as predictions from the HFSS model. There is good agreement over most of the spectrum. HFSS predicts a sharp coupling to surface waves in the standoff at 6.14 µm where the experiment shows that this effect is less concentrated. In both measurement and experiment the resonance of the structure shifts to 9.25 µm under normal incidence. At this wavelength, HFSS predicts a reflectivity of < 0.0001 while we experimentally measure the reflectivity to be 0.015, near the floor of the instrument. This makes the structure a near-perfect absorber at this wavelength. We were unable to measure the angular dependence of the FSS directly, but simulated angular and spectral reflectance is highlighted in Fig. 4(b) and 4(c), which shows the shift in peak absorbance to 10.6 µm under 60° off normal incidence TE illumination. The figure also shows the sharp diffraction edge when the light is TM polarized.
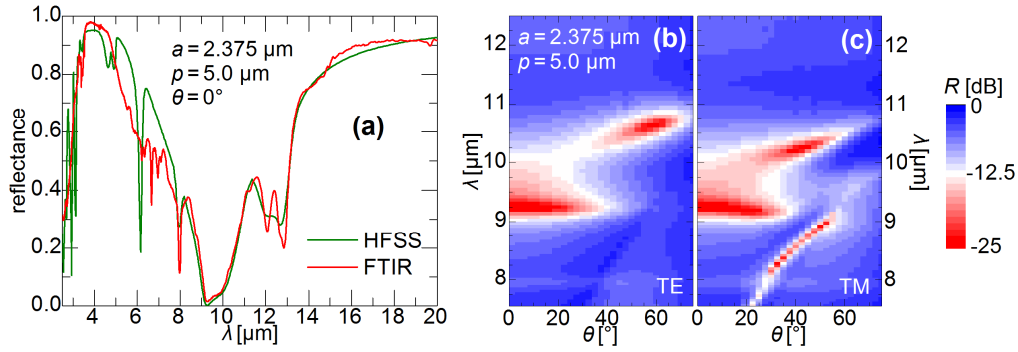
Fig. 4. Far-field reflectivity of an infinite uniform FSS. (a) FTIR measurement and simulation at normal incidence. Simulated (b) TE and (c) TM specular reflectivity as a function of incidence angle and wavelength.

Figure 5 shows the *s*-SNOM results for the uniform-array FSS. The near-field map shows that the elements are in phase with each other. An HFSS simulation of the normal field component, E_z, evaluated 5 nm above the top surface of the elements is shown in Fig. 5(d). Scanning introduces a phase shift in the *y*-direction due to the off-normal illumination in the *yz* plane (see Fig. 2). This does not occur in the SNOM image because the portion of the sample being sampled by the probe is constantly illuminated with the same phase (the beam is focused on the tip). The simulated result has been corrected for this phase shift so that

$$\varphi = \varphi_0 - y \cdot k_0 \cdot \sin\theta \qquad (2)$$

where φ and φ_0 denote the plotted phase and calculated phase respectively. In Figs. 5 and 6 we have employed Eq. (2) to remove the phase shift from the simulation results although it could also be used calculate the true phase from experimental results. When the reference leg is moved $\lambda_0/4$ (the distance the light travels in the reference leg is twice the displacement of the mirror as shown in Fig. 1) the phase is shifted by 180° and the direction of the E-field (+/−) is reversed from Fig. 5(c).
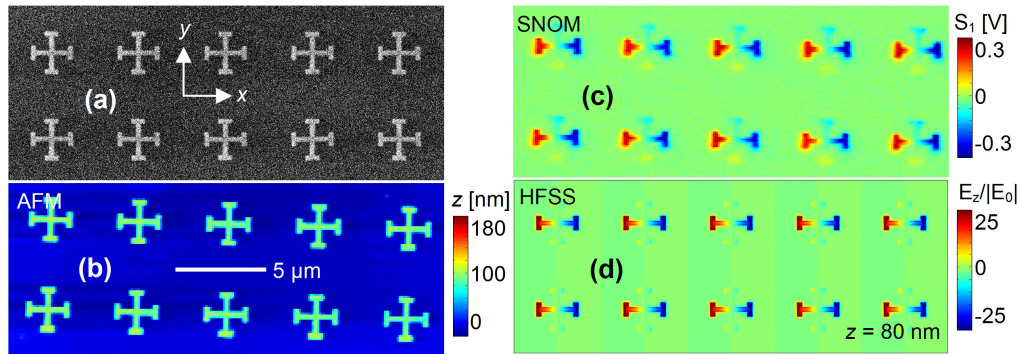

Fig. 5. SNOM results for uniform resonant FSS: (a) SEM image of structure; (b) sample topography from AFM data; (c) measured SNOM signal and (d) HFSS simulation results showing *Ez* after post-processing to account for scanning (Media 1 and Media 2).

Figure 6 shows the *s*-SNOM results for the phase ramp of different sized elements. The phase-resolved field is plotted in Fig. 6(c). In that data set, the reference leg (phase) was adjusted to produce the maximum amplitude at the center (resonant) cross. Figure 6(e) shows the value of the E_z from HFSS. Figures 6(d) and 6(f) show the measured and calculated signals when the reference leg has been moved $\lambda_0/8 = 1.32$ μm (90°). These results qualitatively agree with the experimental results and show that the off-resonant crosses on either side of the resonant structure are out of phase with each other.
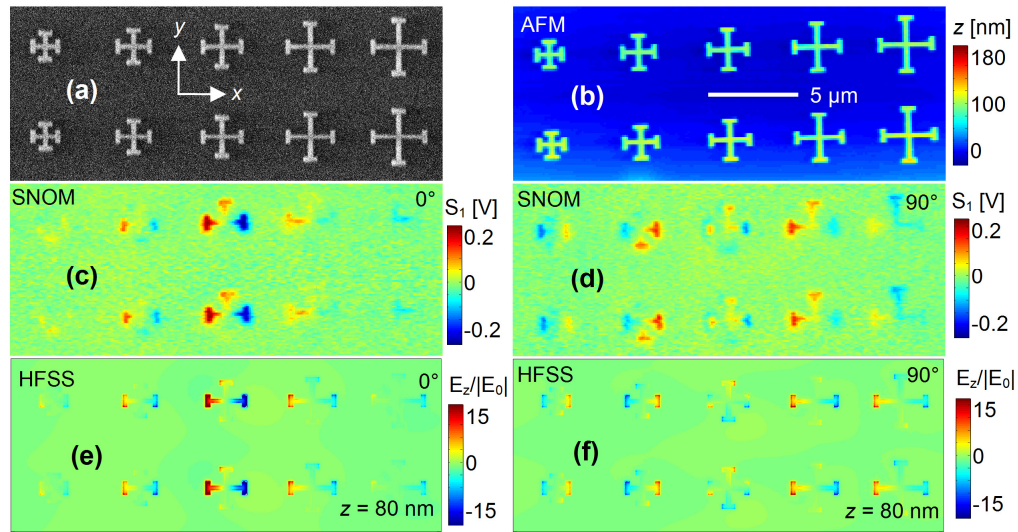
Fig. 6. *s*-SNOM results for phase ramp FSS: (a) SEM image of structure; (b) sample topography from the AFM data; (c) and (d) measured *s*-SNOM signal with reference leg adjusted to maximize signal from center cross and 90° relative phase; (e) and (f) post-processed HFSS simulation results showing E_z at 0 and 90° relative phase (Media 3 and Media 4).

Figure 7 shows *s*-SNOM measurements from a line scan over rows of the elements. Five different rows of elements were scanned. Each row was scanned 25 times at different phases (advanced on a 45° interval), then a least-squares fit was performed to resolve the amplitude and relative phase at each point along the line. The magnitude of the fitted near-field signal along with $|E_z|_{z\,=\,80\,nm}$ from simulation (normalized to the incident field intensity) for the uniform elements is plotted in Fig. 7(a) and for the phase ramp array in Fig. 7(d). The fitted and simulated phases are compared in Figs. 7(b) and 7(e) along the topographies for both samples in Figs. 7(c) and 7(f).
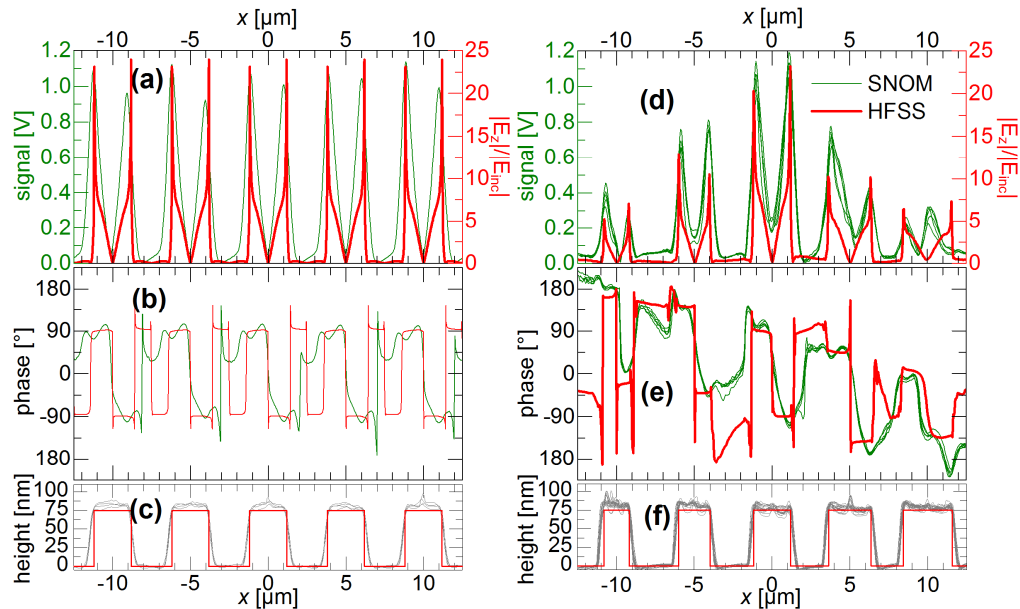
Fig. 7. Comparison between *s*-SNOM and simulation results: (a) normalized magnitude; (b) phase; and (c) topography for the uniform FSS array; (d) normalized magnitude; (e) phase ; and (f) topography for the phase ramp.

There is good agreement between the measured and simulated data, particularly for the uniform elements. As expected the elements are in phase with each other for the uniform sample. For the different-sized elements, the resonant element has the brightest near-field signal. Both simulation and experiment show a phase transition across the pattern with smaller elements leading larger elements. The discrepancies between measured and simulated phase can largely be attributed to self-homodyne interference between the scattered signal and a position-dependent background in addition to the reference leg as well as challenges precisely assigning phase between the structures where the signal amplitude is very low.

5. Conclusion

An FSS consisting of loaded crossed dipole elements was designed, fabricated, and imaged using *s*-SNOM. The structure was designed to have near perfect absorption at normal incidence (9.75 µm) and 60° off normal incidence (10.6 µm). We showed that there is a phase shift for the reflected light for off-resonant elements with simulation and *s*-SNOM measurement. *s*-SNOM enabled access to the near-field phase even though the far-field reflectance was very low. Besides demonstrating utility of *s*-SNOM for studying this type of structure, this work will aid in the design of steerable reflectors with defined directivity at IR and visible frequencies. Beyond model validation, *s*-SNOM will be useful for the case of large semi-periodic or finite arrays that would be computationally difficult to simulate. It also furthers the design and construction of FSS with high absorption.

Acknowledgments